www.afm-journal.de

# Mitigating Pt Loss in Polymer Electrolyte Membrane Fuel Cell Cathode Catalysts Using Graphene Nanoplatelet Pickering Emulsion Processing

Kyu-Young Park, Matthew E. Sweers, Ulrich Berner, Erhard Hirth, Julia R. Downing, Janan Hui, Jonathan Mailoa, Christina Johnston, Soo Kim,\* Linsey C. Seitz,\* and Mark C. Hersam\*

Carbon-supported Pt nanoparticles are the leading catalysts for the cathode oxygen reduction reaction (ORR) in polymer electrolyte membrane fuel cells. However, these ORR catalysts suffer from poor electrochemical durability, particularly the loss of electrochemical surface area (ECSA) due to Pt nanoparticle dissolution and agglomeration. Here, Pt loss is mitigated through a Pickering emulsion-processing strategy that employs graphene nanoplatelet dispersions stabilized by the polymer ethyl cellulose. The resulting graphene-Pt/Vulcan carbon (Pt/C) catalysts exhibit superior durability and ECSA retention throughout an accelerated stress test compared with a commercial Pt/C standard catalyst, both in a diagnostic-rotating disc electrode setup and in a membrane electrode assembly full cell. These graphene-Pt/C catalysts also improve durability at high-voltage conditions, providing further evidence of their exceptional electrochemical stability. Consistent with density functional theory calculations, postelectrochemical characterization reveals that Pt nanoparticles localize at graphene defects both on the basal plane and especially at the edges of the graphene nanoplatelets. Since this Pt nanoparticle localization suppresses Pt nanoparticle dissolution and agglomeration without hindering accessibility of the reactant species to the catalyst surface, the ORR performance under both idealized and practical experimental conditions shows significantly improved durability while maintaining high electrochemical activity.

### 1. Introduction

With accelerating worldwide demand for sustainable energy applications, fuel cell systems have received significant attention as an alternative to combustion-based power generation due to their low environmental impact and high energy density.[1] Among the various classes of fuel cells, the polymer electrolyte membrane fuel cell (also known as the proton exchange membrane fuel cell, PEMFC) has shown high theoretical efficiency up to 80%, high power density up to 0.7 W cm<sup>-2</sup>, low operating temperature below 100 °C, and amenable portability, thus making it is a promising power source for electrified transportation applications.<sup>[2]</sup> The energy efficiency of PEMFCs is governed by the kinetics of the hydrogen oxidation reaction (HOR) and the oxygen reduction reaction (ORR) at the anode and the cathode, respectively. The cathode ORR is widely regarded as the limiting halfreaction for overall PEMFC performance

K.-Y. Park, M. E. Sweers, J. R. Downing, J. Hui, M. C. Hersam Department of Materials Science and Engineering Northwestern University Evanston, IL 60208, USA

E-mail: m-hersam@northwestern.edu

The ORCID identification number(s) for the author(s) of this article can be found under https://doi.org/10.1002/adfm.202205216.

© 2022 The Authors. Advanced Functional Materials published by Wiley-VCH GmbH. This is an open access article under the terms of the Creative Commons Attribution-NonCommercial License, which permits use, distribution and reproduction in any medium, provided the original work is properly cited and is not used for commercial purposes.

[+]Present address: Cell Engineering, Rivian Automotive, 607 Hansen Way, Palo Alto, CA, 94304, USA

DOI: 10.1002/adfm.202205216

Graduate Institute of Ferrous and Energy Materials Technology Pohang University of Science and Technology Pohang, Kyungbuk 37673, Republic of Korea U. Berner, E. Hirth Robert Bosch GmbH Corporate Research Robert-Bosch-Campus 1, 71272 Renningen, Germany J. Mailoa, S. Kim<sup>[+]</sup> Research and Technology Center Robert Bosch LLC 1 Kendall Square Suite 7–101, Cambridge, MA 02139, USA E-mail: sookim@rivian.com C. Johnston

Research and Technology Center Robert Bosch LLC 384 Santa Trinita Ave, Sunnyvale, CA 94085, USA www.advancedsciencenews.com

ADVANCED FUNCTIONAL MATERIALS

www.afm-journal.de

due to its sluggish four-electron transfer process.<sup>[3]</sup> Therefore, durable and electrochemically active ORR catalysts are essential for high-performance PEMFC technology.

Carbon-supported precious metal nanoparticles are leading electrocatalysts in incumbent PEMFC electrodes for both HOR and ORR. In particular, Pt nanoparticles provide relatively straightforward synthesis, high reliability, and superior energy conversion efficiency over 40%,[4] making them the most commonly employed catalysts for PEMFCs.<sup>[5]</sup> However, Ostwald ripening, [6] dissolution, [7] and contamination of active sites, [8] caused by the thermodynamic instability of Pt nanoparticles lead to significant decreases in electrochemical surface area (ECSA) and increased overpotentials during electrochemical cycling. Moreover, loss of catalytic activity and carbon support corrosion caused by the highly oxidizing conditions during electrochemical cycling further exacerbate the degradation of these Pt nanoparticle catalysts and can also lead to their physical detachment from the electrode. [7] The limited availability of precious metal catalysts is also a key consideration for practical PEMFC applications. Although the typical PEMFC anode requires low loadings of Pt nanoparticles (typically less than 0.05 mg cm<sup>-2</sup>), PEMFC cathodes require up to one order of magnitude higher Pt nanoparticle loadings due to their inferior ORR kinetics.<sup>[9]</sup> This high Pt nanoparticle loading on the cathode results in Pt being the largest contributor to the cost of PEMFC stacks and a nontrivial cost contributor for the entire fuel cell.[10]

In order to improve electrochemical performance and thus reduce the requisite loading of Pt nanoparticles, it is essential to design ORR cathodes with high catalytic activity and durability upon long-term usage. A common approach in pursuit of this goal is to employ high surface area carbon support materials with Pt nanoparticles in the micropores. The resulting spatially distributed nanoparticles can inhibit Pt nanoparticle coarsening, resulting in enhanced ECSA stability.[11] Additional strategies include encapsulation and anchoring designs for the Pt nanoparticles.<sup>[12]</sup> Encapsulation attempts to stabilize the surface of the Pt nanoparticles, which improves resistance against dissolution, aggregation, and chemical degradation.[12b,f,13] For example, carbon shells have been shown to enhance the durability of Pt nanoparticles, following the accelerated stability test (AST) cycling.[12b] On the other hand, anchoring involves a support that has higher electrochemical or chemical resistance than conventional carbon supports, thus increasing overall stability of the electrode. [12d,e,14] Strong bonding between the support material and Pt nanoparticles can also suppress agglomer-

L. C. Seitz
Department of Chemical and Biological Engineering
Northwestern University
Evanston, IL 60208, USA
E-mail: linsey.seitz@northwestern.edu
M. C. Hersam
Department of Chemistry
Northwestern University
Evanston, IL 60208, USA
M. C. Hersam
Department of Electrical and Computer Engineering
Northwestern University
Evanston, IL 60208, USA

ation, resulting in high ECSA retention upon cycling. The most commonly used materials for encapsulation and anchoring are carbon and oxide materials due to their electrochemical and chemical durability.<sup>[15]</sup>

While these tailored cathode designs have improved ORR electrochemical performance and lifespan, their complex processing conditions have been difficult to translate from laboratory-scale demonstrations to large-scale production. Moreover, if the active sites of the Pt nanoparticles are fully embedded in an exterior coating, then improved durability comes with a tradeoff in catalytic activity. Therefore, a need remains for alternative PEMFC cathode design strategies that have wide versatility, ease-of-synthesis, and reproducibility, while improving electrochemical durability without compromising electrochemical performance. Toward this end, here, we employ a scalable Pickering emulsion catalyst-processing strategy that employs graphene nanoplatelet dispersions stabilized by the polymer ethyl cellulose (EC). Following thermal decomposition and removal of the EC, the resulting graphene-Pt/Vulcan carbon (Pt/C) catalysts demonstrate superior durability and ECSA retention compared with a commercial Pt/C standard catalyst, particularly at high-voltage conditions. Direct observation of the electrode after 30 000 AST cycles confirms the retention of Pt nanoparticles on graphene defects and edges. This experimental result is consistent with density functional theory (DFT) calculations that suggest strong interactions between Pt nanoparticles and graphene defects that are especially prevalent at the edges of graphene nanoplatelets. Further assessment in membrane electrode assembly (MEA) full cells with performance measurements under realistic conditions and an accelerated stress test that correlates well with real drive cycles[16] confirms that the electrochemical durability and performance improvements observed in diagnostic AST testing are maintained in practical conditions. Overall, by localizing Pt nanoparticles in a manner that does not limit accessibility to reactant and product species, this Pickering emulsion-processing strategy concurrently achieves high ECSA and long-term durability in both idealized and practical PEMFC experimental conditions.

# 2. Results and Discussion

The graphene-encapsulated Pt/C catalysts were prepared by adapting a scalable Pickering emulsion process that was originally developed for lithium-ion battery materials.[17] The graphene powder, produced by liquid-phase exfoliation, was dispersed in acetonitrile at a 0.275 mg mL<sup>-1</sup> concentration. To improve the dispersion stability, EC powder equivalent to twice the mass of graphene was homogenized simultaneously.[18] Commercially available Pt/C catalyst particles (Tanaka, TEC10V20E, 20 wt% of Pt nanoparticles on Vulcan carbon) were then mixed into the graphene-acetonitrile solution (Figure 1a, left) with a 10:1 w/w ratio of Pt/C to graphene (the nominal final Pt content is 18.2 wt%). Then, hexane with 20% of the volume of the acetonitrile solution was added to form the Pickering emulsion. Once the emulsion was formed, the evenly mixed graphene and Pt/C powders sedimented to the bottom of the beaker as shown in the inset photo of Figure 1a (right). This sedimentation is consistent with observations from the

16163028, 2022, 43, Downloaded from https://onlinelibrary.wiley.com/doi/10.1002/adfm.202205216 by University Of Chicago Library, Wiley Online Library on [06/11/2022]. See the Terms

zonditions) on Wiley Online Library for rules of use; OA articles are governed by the applicable Creative Commons I

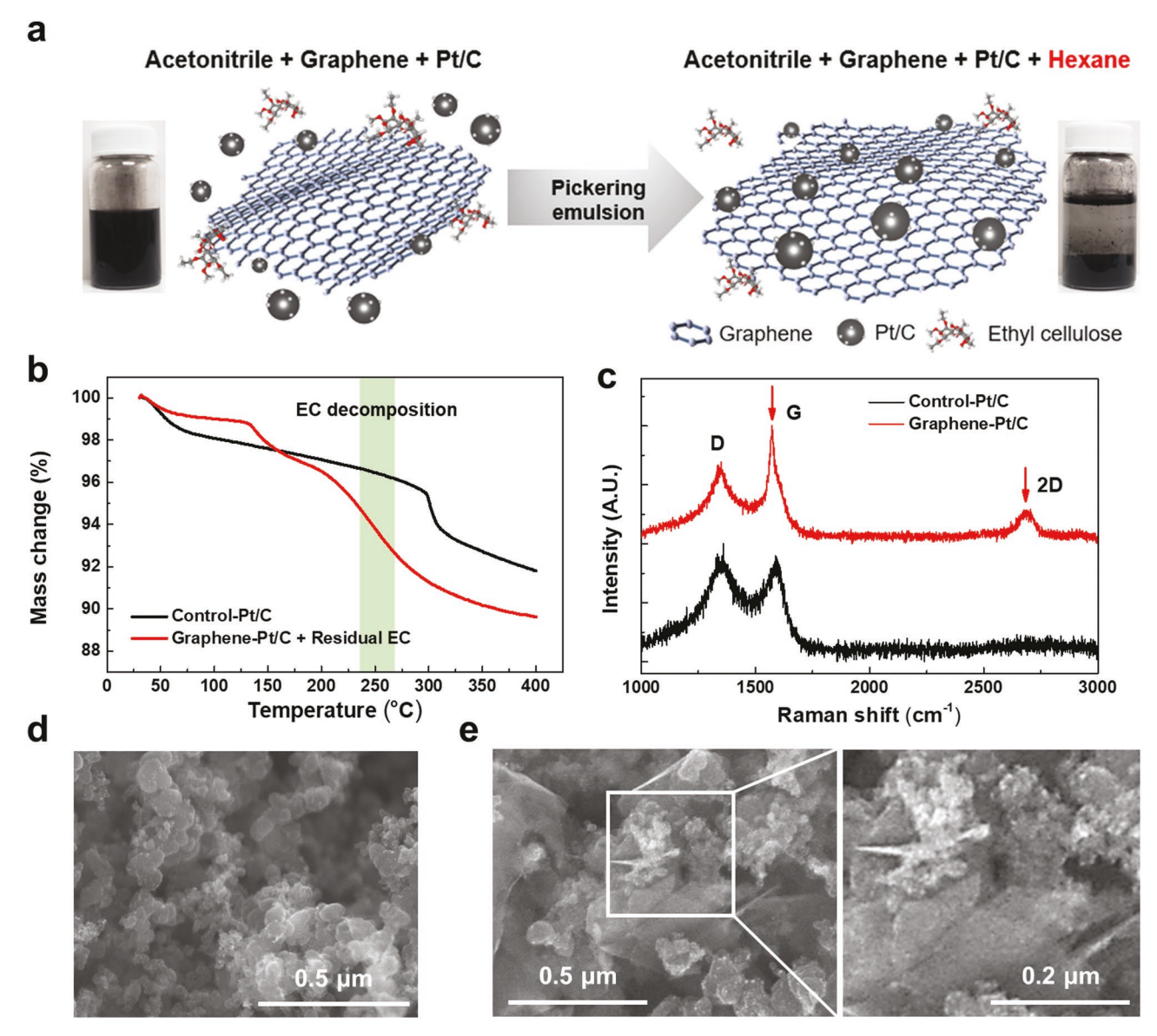


Figure 1. Synthesis method and sample characterization. a) Pickering emulsion-processing schematic. b) TGA for the control-Pt/C catalyst and the graphene-Pt/C composite with residual EC. c) Raman spectra of the control-Pt/C catalyst and the graphene-Pt/C composite. d,e) SEM images of the (d) control-Pt/C catalyst and (e) graphene-Pt/C composite after completing the Pickering emulsion process.

Pickering emulsion process originally developed for lithium-ion battery materials, [17] indicating that an evenly mixed graphene-Pt/C composite was produced. Hexane was then evaporated first by fractional distillation, and the final graphene-Pt/C composite powder was obtained by a filtration and drying process (more details of the Pickering emulsion processing are provided in the Methods section and in a previous report<sup>[17]</sup>).

Residual EC polymer was removed from the powder mixture by thermal curing at a temperature of 250 °C for 10 min in a nitrogen atmosphere. Figure 1b shows thermogravimetric analysis (TGA) results for the control-Pt/C catalyst compared with the graphene-Pt/C composite with residual EC. The control-Pt/C catalyst had a major mass change at 100 °C due to water evaporation and subsequently a small mass change of 3% at 300 °C. Meanwhile, the graphene-Pt/C composite with residual

EC showed its first mass change near 120 °C, presumed to be evaporation of residual Pickering emulsion solvents, and then exhibited a significant mass change of more than 8% at 250 °C (green-colored region in Figure 1b). This mass change behavior is consistent with previous cases that also removed EC by thermal curing. [17] The cured graphene-Pt/C composite was analyzed with Raman spectroscopy (Figure 1c) and scanning electron microscopy (SEM, Figure 1d,e and Figure S1, Supporting Information). As shown in Figure 1c, additional G and 2D bands are observed at 1600 and 2700 cm<sup>-1</sup> (red arrows, additional sharp peak of the G band and new peak of the 2D band), respectively, in the cured graphene-Pt/C composite powder, which confirms the presence of graphene. [19] SEM images of the control Pt/C powder (Figure 1d) show the typical round shape of Vulcan carbon, whereas the Pickering

16163028, 2022, 43, Downloaded from https://onlinelibrary.wiley.com/doi/10.1002/adfm.202205216 by University Of Chicago Library, Wiley Online Library on [06/11/2022]. See the Terms and Conditions (https://onlinelibrary.wiley.

conditions) on Wiley Online Library for rules of use; OA articles are governed by the applicable Creative Commons I

www.advancedsciencenews.com www.afm-journal.de

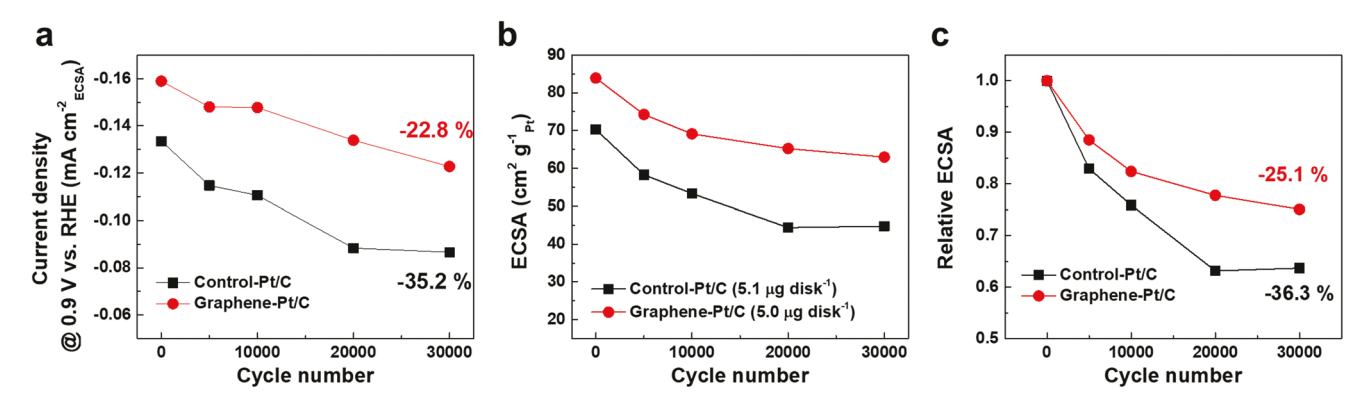


Figure 2. Extended ORR testing up to 30 000 cycles between 0.6 and 0.95 V versus RHE. a) ECSA-normalized activity, b) absolute ECSA values, and c) relative ECSA change as a function of cycle number.

emulsion sample shows graphene nanoplatelets being homogeneously blended with the Pt/C catalyst without segregation as shown in Figure 1e. In addition, no significant change in the size of the Pt nanoparticles was observed in SEM (Figure S2, Supporting Information), although particle size estimates from powder X-ray diffraction (PXRD, Figure S3, Supporting Information) indicated a slight increase of the Pt nanoparticle size from 3.1 nm (control) to 5.4 nm (graphene-Pt/C), which can be attributed to the graphene-Pt/C thermal-processing conditions. Further characterization using transmission electron microscopy (TEM) images in Figure S4 (Supporting Information) also confirms that the graphene flakes are well distributed in the composite mixture with minimal Pt nanoparticle aggregation.

Following an initialization step, extended potential cycling in a rotating disc electrode (RDE) between 0.6 and 0.95 V versus a reversible hydrogen electrode (RHE) reveals higher ORR activity in the form of higher beginning of life (BoL) ECSA for the graphene-Pt/C composite compared with the control-Pt/C powder. In addition, the graphene-Pt/C composite achieves improved stability with the half-wave potential (E<sub>1/2</sub>) only decreasing by 31 mV after 30 000 cycles compared with the control-Pt/C powder that decreases by 47 mV after the same number of cycles (Figure S5, Supporting Information). Similarly, the ECSA-normalized current density at 0.9 V versus RHE only decreases from –159 to –123  $\mu A$  cm $^{-2}_{ECSA}$  (–22.8%) for the graphene-Pt/C composite in comparison to the decrease from -134 to  $-87~\mu A~cm^{-2}_{ECSA}$  (-35.2%) for the control-Pt/C powder (Figure 2a). In addition, Figure 2b shows that the graphene-Pt/C composite displays higher postinitialization ECSA (77.5 m<sup>2</sup> g<sup>-1</sup><sub>Pt</sub>) than the control-Pt/C powder (68.9 m<sup>2</sup> g<sup>-1</sup><sub>Pt</sub>). The graphene-Pt/C composite also retained a larger fraction of its active surface area during extended durability testing, losing only 25.1% of ECSA compared with 36.3% for the control-Pt/C powder after 30 000 cycles as shown in Figure 2c. It is worth noting that the electrodes prepared by the Pickering emulsion method showed higher ECSA with relatively low ECSA loss after cycling compared with previous reports using graphene-based substrates (Table S1, Supporting Information). In these previous studies, graphene has primarily been used as a supporting substrate, whereas the Pickering emulsion method employs graphene as a relatively low-loading additive to enhance the electrochemical properties of the catalyst.

Microscopic observation of the electrodes reveals that the graphene nanoplatelets mitigate Pt loss during cycling by providing redeposition and localization sites for Pt nanoparticles. Figure 3a shows SEM images of the graphene-Pt/C composite as a function of cycle number. Although Pt nanoparticles are not observed on the graphene nanoplatelets in the initial state (0 cycle), they become apparent on the graphene nanoplatelets after the initialization step (see white arrows). Throughout the 30 000 cycles, the size and number of Pt nanoparticles continuously increase in abundance on the graphene nanoplatelets, and they preferentially form at the edges of graphene nanoplatelets (Figure 3a) rather than on the graphene basal plane, which is the first indication that deviations from the pristine graphene structure provide localization sites for Pt nanoparticle redeposition (additional SEM, energy-dispersive X-ray analysis, and TEM results are provided in Figures S6-S9, Supporting Information). This observation provides a clear explanation for the higher ORR activity and durability of the graphene-Pt/C composite compared with the control-Pt/C powder since the graphene nanoplatelets suppress Pt loss during the initialization step and extended AST cycling.

First-principles DFT calculations with van der Waals inclusive functionals provide an explanation for Pt localization at graphene defects. First of all, multiple graphene nanoplatelet models using 48 carbon atoms with hydrogen-passivated and unpassivated (i.e., H vacancies) edge atoms were considered to mimic the graphene edges in the graphene-Pt/C composite (Figure S10, Supporting Information). We find that Pt can bind favorably with a DFT-calculated binding energy of -0.954 eV (Figure 3b) at graphene edge sites (e.g., Figure S10c, Supporting Information), where we used the bulk face-centered cubic Pt atom as the reference energy. Moreover, certain inplane vacancy defects (e.g., graphene quad-vacancies (QVs)) also provide localization sites for Pt atoms while allowing the transport of the fuel cell reactants and products (i.e., H2, O2, and H2O do not bind with the graphene QV defect as shown in the relative DFT-binding energy calculations provided in Figures S10-S16, Supporting Information). Figure 3c displays the relative binding energy change in units of eV when Pt moves toward the QV defect in the z-direction from the vacuum (schematic side and top views are shown in the inset). In this calculation, we set the reference energy as 0 eV when a Pt atom is far away from the graphene sheet (i.e., ≈7 Å away from the

-and-conditions) on Wiley Online Library for rules of use; OA articles are governed by the applicable Creative Commons I

www.afm-journal.de

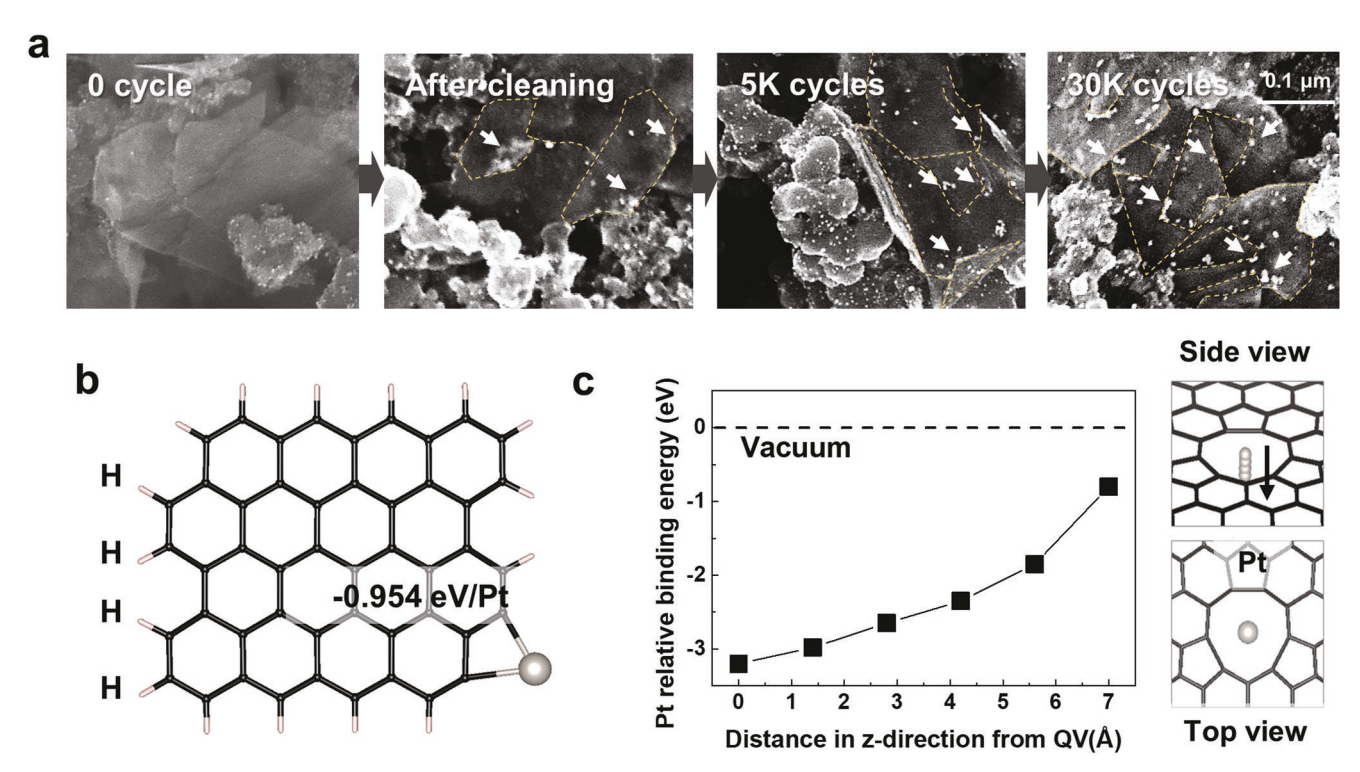


Figure 3. Pt nanoparticle redeposition and localization on graphene nanoplatelet defects. a) SEM observation for the graphene-Pt/C composite after 0 cycles, after electrochemical initialization (cleaning), after 5000 cycles, and after 30 000 cycles in the RDE. b) DFT-binding energy calculation for graphene sheet with edge defect with an adsorbed Pt atom (using Pt bulk atom as the reference energy). c) Relative DFT-binding energy as a function of distance between Pt atom at vacuum, moving toward the graphene basal plane QV defect. Inset figures: Side view and top view of the DFT calculation model.

graphene sheet in the *z*-direction). As the Pt moves closer to the QV, the relative binding energy becomes more negative (i.e., Pt binds favorably to the graphene defects, when compared with vacuum). From our DFT calculations, we show that graphene defects, either at the nanoplatelet edge sites or in-plane defects, provide localization sites for Pt, which leads to sustained electrochemical activity upon extended cycling.

Our experimental observations show that the preferred Pt redeposition location is at graphene nanoplatelet edges, which provide a higher concentration of localization sites than the graphene basal plane.<sup>[18]</sup> Moreover, this conclusion agrees well with previous experimental observations that edge defects are commonly observed in graphene nanoplatelets, but large multivacancy defects on the basal plane are relative rare, [20] resulting in overall edge preference for Pt nanoparticle redeposition (Figures S8 and S9, Supporting Information). For further discussion on the in-plane defect formation energy, please refer to the DFT results in Table S1 (Supporting Information). We also expect that under ORR conditions, the oxidative potentials disrupt the hydrogen termination at the edge sites, resulting in a higher incidence of edge defects than can serve as Pt nanoparticle redeposition sites. In addition to providing sites for Pt nanoparticle localization, the graphene-Pt/C composite possesses a relatively open structure, as opposed to a conformally coated or wrapped structure (see SEM image of Figure 1e). This open structure is beneficial for facilitating transport of H<sub>2</sub>, O<sub>2</sub>, and H<sub>2</sub>O, which is necessary for high electrochemical activity. However, once Pt diffusion initiates at harsh operating conditions, the graphene nanoplatelets provide localization sites due to a strong Pt attraction, thus minimizing Pt loss and transport into other cell components.

More aggressive electrochemical testing of the graphene-Pt/C composite reveals similar trends at high potential conditions as shown in Figure 4 and Table 1. Following a combination of high-voltage cycling and a shortened AST protocol (HVAST, 1.0-1.5 V vs RHE, 1000 cycles), the graphene-Pt/C composite displays high initial ECSA (77.5 m<sup>2</sup> g<sup>-1</sup><sub>Pt</sub>) and high durability (11% loss), both of which are superior to the Pt/C control powder. The ORR activity is also superior for the graphene-Pt/C composite with the geometric current density at 0.9 V versus RHE starting at -1.30 mA cm<sup>-2</sup><sub>geo</sub> (-1.06 mA cm<sup>-2</sup><sub>geo</sub>) and decreasing by 12% (14%) for the composite (control). The high overpotential region (0.5-0.8 V vs RHE) for the Pt/C control powder also exhibits a significant reduction in current density after high potential cycling, even though the mass transport limited current is similar. The same current loss is not observed for the graphene-Pt/C composite, which retains the line shape of its initial polarization curve.

This durability at high potentials stems from not only from Pt nanoparticle localization on the graphene nanoplatelets but also reinforced Vulcan carbon stability. Compared with pristine, uncycled Pt/C powder (Figure 4c), the Pt/C control powder following exposure to high potential conditions shows corrosion behavior in the form of increased size of Vulcan carbon. [21] Meanwhile, the Vulcan carbon in the graphene-Pt/C composite electrode remains relatively intact with its original shape

16163028, 2022, 43, Downloaded from https://onlinelibrary.wiley.com/doi/10.1002/adfm.202205216 by University Of Chicago Library, Wiley Online Library on [06/11/2022]. See the Terms and Conditions (https://onlinelibrary.wiley.com/rerms

-and-conditions) on Wiley Online Library for rules of use; OA articles are governed by the applicable Creative Commons I

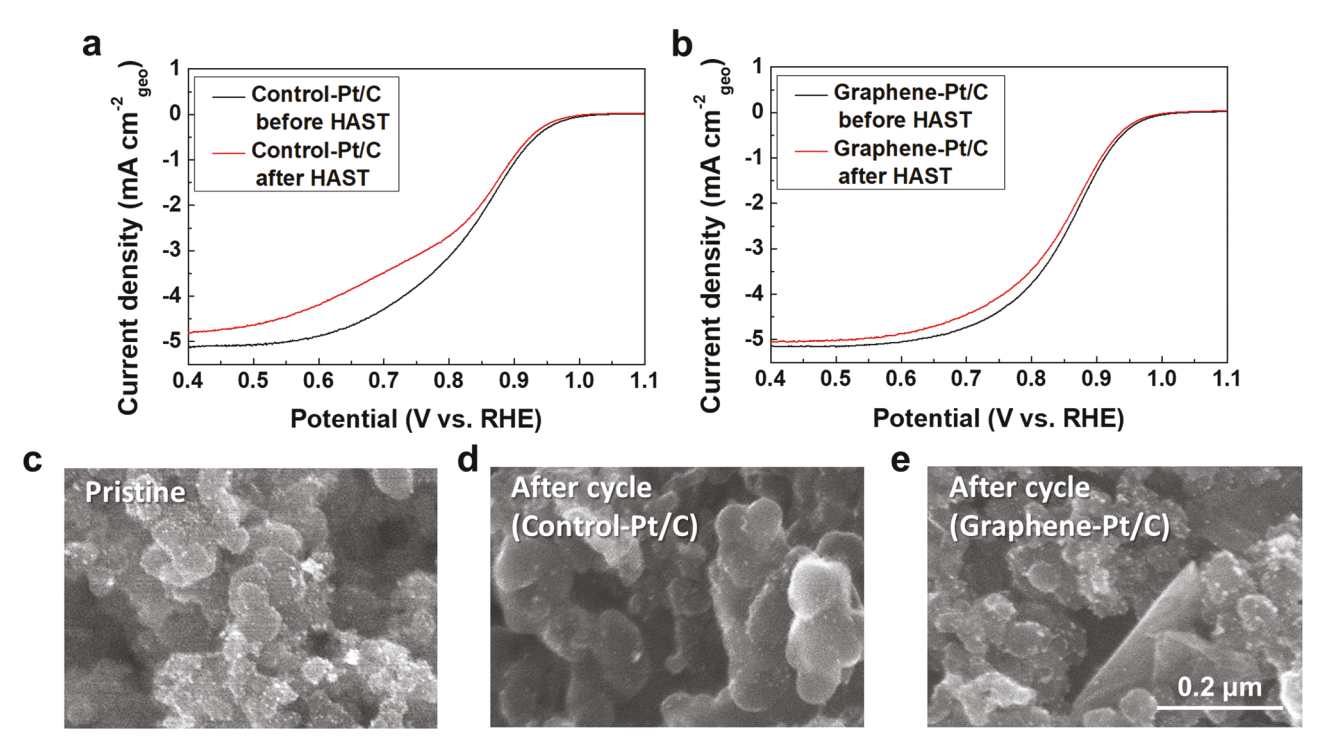


Figure 4. High-voltage AST test results in the RDE. ORR activity changes before and after the high-voltage AST test for: a) control-Pt/C catalyst and b) graphene-Pt/C composite. SEM images of: c) pristine and d) control-Pt/C catalyst after high-voltage AST, and e) graphene-Pt/C composite after high-voltage AST.

maintained even after high-potential exposure. One possible explanation is that the Vulcan carbon stability is enhanced by the EC treatment. According to our previous work, the curing that removes EC leads to notable reductions in the D/G intensity ratio in Raman spectra, indicating high  $sp^2$ -bonding in the residual carbon following EC decomposition. [22] Similarly, the Pickering emulsion processing that includes EC thermal curing provides an enrichment of  $sp^2$ -bonded carbon that enhances the durability of Vulcan carbon at high potentials. Moreover, the high electrochemical stability and electrical conductivity of graphene provide the added benefit of maintaining electron percolation pathways throughout extended electrochemical cycling. [23]

To determine if the graphene-Pt/C composites provide similar benefits in real-world conditions, additional measurements were performed in fully assembled MEA fuel cells using commercially relevant testing protocols. In this case, the cathodes were produced using the same Pt/C control powders and graphene-Pt/C composites as in the RDE testing but with an intermediate ink coating and decal transfer step on an 8  $\mu m$  membrane. The cathode loadings were fixed at 0.13  $mg_{Pt}$  cm $^{-2}$ .

Polarization data and cyclic voltammograms (CVs) of the MEA full cells were measured at BoL and after an accelerated potential cycling stress test between 0.6 and 1 V (vs the anode) with 6000 cycles. Figure 5a shows the polarization data at BoL and at the end of test (EoT). As shown in Figure 5a,b, the BoL data of both the Pt/C control powders and graphene-Pt/C composites are comparable, but the durability of the Pt/C control powders is significantly lower than the graphene-Pt/C composites, with a potential drop in the kinetic region (25–50 mA cm<sup>-2</sup> region) of ≈30 mV for the graphene sample, whereas the control shows a 45 mV decrease. Both catalyst materials have a BoL ECSA in range of 67-70 m<sup>2</sup> g<sup>-1</sup>, which agrees well with other literature examples using the same Pt/C catalyst material, [24] but the ECSA only decreases by 60% for the graphene-Pt/C composite compared with 74% for the Pt/C control powder during the stress test. These ECSA changes correlate well with the observed potential decrease in the kinetic region, indicating that the reduction in Pt surface area is the main degradation mechanism. The CVs measured during the stress test are shown in Figure S14 (Supporting Information). Interestingly, for the graphene-Pt/C composite, the CV peak around 0.25 V

 Table 1. Comparison of high-voltage AST results.

Sample	ECSA after cleaning [m² g <sup>-1</sup> ]	ECSA after HVAST [m² g <sup>-1</sup> ]	ECSA changes [%]	Current density @ 0.9 V after cleaning [mA cm <sup>-2</sup> geo]	Current density @ 0.9 V after HVAST [mA cm <sup>-2</sup> geo]	Activity changes [%]
Control-Pt/C	69	58	-16	-1.06	-0.91	-14
Graphene-Pt/C	80	70	-11	-1.30	-1.14	-12

16163028, 2022, 43, Downloaded from https://onlinelibrary.wiley.

com/doi/10.1002/adfm.202205216 by University Of Chicago Library, Wiley Online Library on [06/11/2022]. See the Terms

ons) on Wiley Online Library for rules of use; OA articles are governed by the applicable Creative Commons I

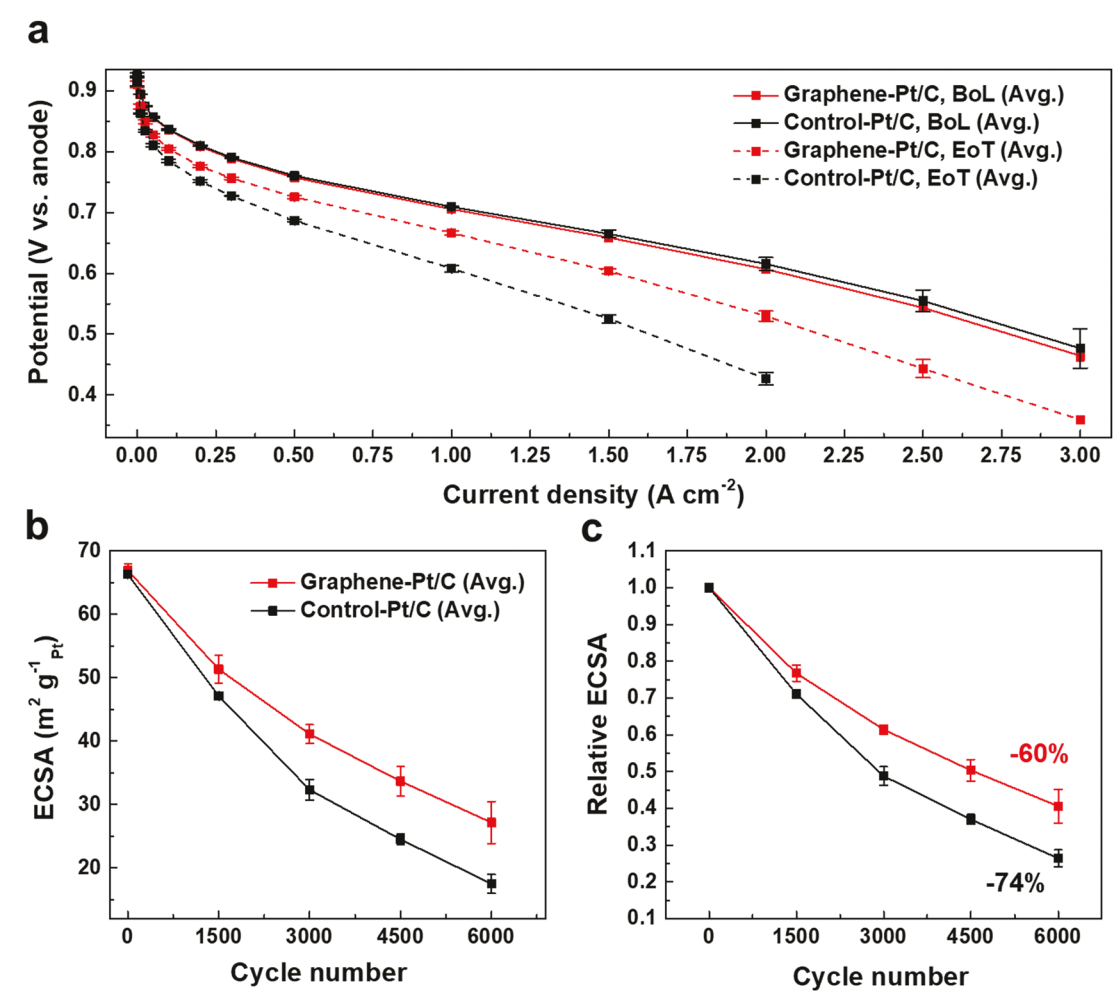


**Figure 5.** MEA full-cell electrochemical performance testing with the graphene-Pt/C composite and the control-Pt/C catalyst. a) Polarization data before and after 6000 cycles. AST conditions: 0.6-1.0 V cycling at 80 °C and 100% relative humidity (RH) in  $H_2/N_2$ . UI conditions: 80 °C, RH = 70%/70% (anode/cathode), lambda = 1.3/1.8 (anode/cathode), p = 2.2/2 bara (anode/cathode). b) Absolute and c) relative ECSA changes as a function of cycle number.

(vs the anode) corresponding to the Pt(100) facet<sup>[25]</sup> increases with cycling (Figure S15, Supporting Information), which is most likely due to the newly formed Pt nanoparticles on the graphene nanoplatelets (Figure S16, Supporting Information). This observation agrees well with a previous report of Pt(100) epitaxially growing on graphene, deviating from the most stable Pt(111) face-centered cubic crystal orientation.<sup>[26]</sup> Overall, these results for the MEA full cells are consistent with the RDE measurements, thus highlighting that the benefits of the graphene-Pt/C composite translate to real-world conditions with promising implications for commercial fuel cell applications.

## 3. Conclusion

Pt nanoparticles on carbon supports are the leading ORR catalyst material in PEMFCs due to their many practical attributes, but their limited electrochemical durability resulting from Pt nanoparticle instability has represented a clear bottleneck for widescale adoption of this clean energy technology. In this work,

we have addressed this issue by employing a scalable Pickering emulsion-processing strategy that yields homogeneously blended graphene nanoplatelets with Pt/C catalyst particles. The resulting graphene-Pt/C composites exhibit superlative ECSA and ORR activity retention both in idealized RDE tests and practical MEA full cells. By comparing experimental observations and theoretical calculations, this improved electrochemical performance can be attributed to Pt nanoparticle redeposition and localization at defect sites on the graphene nanoplatelets. In particular, graphene nanoplatelet edge sites and basal plane vacancy defects provide thermodynamically favorable binding sites for Pt, efficiently mitigating Pt loss, and improving durability. Moreover, the graphene-Pt/C composite provides an open microstructure, resulting in minimal barriers for reactants to reach and products to leave catalytically active sites, which leads to high initial ECSA and ORR activity. High ORR activity and durability are maintained at high potentials not only due to Pt localization on graphene nanoplatelets but also because of the high sp<sup>2</sup>-bonding character of the carbon residue, following EC thermal curing that minimizes corrosion of the Vulcan carbon support. Since this

ADVANCED FUNCTIONAL MATERIALS

www.advancedsciencenews.com www.afm-journal.de

approach utilizes scalable solution processing and results in high performance in real-world testing conditions, it holds promise for accelerating the adoption of PEMFC technology in clean energy applications.

# 4. Experimental Section

Graphene Preparation: Graphene flake powder was obtained by solution-based exfoliation of graphite. In particular, 6 kg of graphite (Sigma-Aldrich) and 200 g of ethyl cellulose (4 cP, Sigma-Aldrich) were mixed in 5 L of ethanol (200-proof, Decon Labs, Fisher Scientific). The resulting solution was continuously agitated by a shear mixer (Silverson Machines) for 24 h. Subsequently, the mixture was centrifuged at 6500 rpm for 30 min using a JLA 8.1000 rotor (Beckman Coulter). The supernatant solution containing graphene and ethyl cellulose was carefully collected, and a NaCl aqueous solution was added for flocculation. The sedimented solids were collected by filtration and washed with deionized water three times to remove residual NaCl salt. The resulting graphene/ethyl cellulose mixture was dried under an infrared lamp overnight.

Pickering Emulsion Processing: Graphene and ethyl cellulose with a 1:2 weight ratio were dispersed in acetonitrile with a graphene concentration of 0.275 mg mL<sup>-1</sup> via horn sonication for 1 h. Subsequently, 275 mg of 20 wt% Pt/Vulcan C powder (TEC10V20E, Tanaka Kikinzoku KogyoK.K., TKK) was added per 100 mL (i.e., 27.5 mg of graphene) of the prepared graphene acetonitrile dispersion, and hexane was consecutively mixed with a 1:5 ratio of hexane and acetonitrile to form a Pickering emulsion. After forming the emulsion by vortexing for 5 min, the hexane solvent was removed by fractional distillation. Then, the mixture solution was filtered to extract the Pt/C composite containing graphene and ethyl cellulose. The obtained powder was dried in an 80 °C oven for 90 min, followed by removal of residual ethyl cellulose through thermal annealing at 250 °C for 10 min in a nitrogen atmosphere.

Sample Characterization: Sample morphology was imaged by scanning electron microscopy (Hitachi SU8030), and thermogravimetric analysis was carried out using a Mettler Toledo TGA/DSC 3+. Raman spectroscopy was performed using a Horiba Xplora system with an acquisition range from 1000 to 3000 cm<sup>-1</sup>. X-ray diffraction was conducted using the Rigaku Ultima instrument, and fitting was conducted using the GSAS-II software.

RDE Electrochemical Analysis: Catalyst inks were formulated by mixing 5 mg of the catalyst powder into a 3:2:0.05 ratio of MilliQ water, isopropyl alcohol, and Nafion-117. The mixture was then sonicated for 30 min, and electrodes were prepared by dropcasting 10 µL of ink onto a polished glassy carbon disk (5 mm diameter) to target a catalyst loading of 25 μg<sub>Pt</sub> cm<sup>-2</sup> (ICP-OES data are provided in Table S4, Supporting Information). Electrodes were left to dry overnight before electrochemical testing. The electrochemical behavior of the graphene-Pt/C composite was tested using an RDE (Pine Research Instrumentation) in a standard 3-electrode cell, with Pt wire and Ag/AgCl (4 M KOH) as counter and reference electrodes, respectively. All tests were conducted using  $0.1~\mbox{m}$ HClO<sub>4</sub>. Each sample was electrochemically initialized by performing CVs in Ar-purged electrolyte between 0.03 and 1.2 V versus RHE at 50 mV  $\mbox{s}^{-1}$ until the CVs were stable, which was approximately 100 cycles. ECSA was measured using the hydrogen underpotential deposition method (H<sub>UPD</sub>) at 50 mV s<sup>-1</sup>. ORR activity was assessed at 1600 rpm at room temperature with CVs from 0.05 to 1.0 V versus RHE at 10 mV s<sup>-1</sup> in O<sub>2</sub>purged electrolyte. The anodic sweeps were post-IR corrected at 100% using the series resistance determined from impedance spectroscopy, and the background current measured in Ar-purged electrolyte was subtracted. The mass activities of the prepared samples are provided in Table S5 (Supporting Information). Catalyst durability was evaluated with AST by applying a 3s/3s square-wave potential profile stepping between 0.6 and 0.95 V versus RHE for 30 000 cycles in Ar-purged electrolyte. ORR activity and ECSA were measured after 5000, 10 000, 20 000, and 30 000 cycles. Commercial Pt/C catalysts powders (20 wt% Pt, TKK) were

also tested using identical procedures. In order to ensure the stability of the Ag/AgCl reference electrode in the 0.1 M HClO<sub>4</sub> electrolyte, the authors performed electrode calibration measurements before and after AST cycling (Figure S20, Supporting Information).

To test the high-voltage durability of the graphene-Pt/C composite, ECSA and ORR activity were measured before and after consecutive sets of CVs: (a) between 0.6 and 1.0 V versus RHE at 80 mV s<sup>-1</sup> for 5000 cycles; (b) between 1.0 and 1.5 V versus RHE at 500 mV s<sup>-1</sup> for 1000 cycles, both in  $O_2$ -purged 0.1 M  $H_2SO_4$ .

MEA Full-Cell Preparation: MEA experiments were conducted on 25 cm<sup>2</sup> active area. The catalyst-coated membranes (CCMs) were produced using the decal transfer method. Catalyst inks were prepared by mixing the catalyst powders with Nafion ionomer in a water-solvent dispersion (Nafion D2020). On the cathode, a commercial 20 wt% Pt/Vulcan powder (TEC10V20E, Tanaka Kikinzoku KogyoK.K., TKK) and the same material with graphene were used. For the anodes, Umicore catalyst powder was chosen (ELYST PT200390). For the ink synthesis, the powder and the solvent/ionomer mixture were combined with an I/C ratio of 0.8 with a final ink composition of 6.4 wt% catalyst, 4.4 wt% ionomer, 42.5 wt% water, and 46.5 wt% 1-propanol. The ink was dispersed in a ball mill for 2 h at 3000 rpm, followed by coating on a polytetrafluoroethylene sheet using a blade coater (TQC) with an applicator by Zehntner. The final CCMs were assembled by hot pressing both catalyst decals on an 8 μm membrane (Gore) at 150 °C in a roll-laminator. The loadings were estimated by weighing and found to be 0.05  $\pm$  0.01 mg cm<sup>-2</sup> on the anode and  $0.13 \pm 0.01$  mg cm<sup>-2</sup> on the cathode for all samples. For the MEA assembly, a gas diffusion layer (GDL) was placed on both electrodes (anode: AVCarb GDS3250, cathode: AVCarb MB30).

MEA Electrochemical Analysis: The MEA full cells were evaluated in a Baltic FuelCells quickConnect® cell holder with graphite serpentine channel flow fields. The characterization procedure was carried out independently on two control samples and three graphene-Pt/C composite samples using FuelCon Evaluator C10 test benches. In the first step, the MEA full cells were conditioned by 120 cycles between 1.3 A cm<sup>-2</sup> and an air starve (0 V) for 60 and 45 s, respectively. Polarization data was measured at 80 °C, RH = 70%/70% (anode/cathode), lambda = 1.3/1.8, and outlet pressures of 2.2/2 bara, for anode/cathode, respectively. CVs of the cathode were measured at 80 °C between 0.07 and 0.9 V with a scan rate of 50 mV s<sup>-1</sup> and ambient pressure in H<sub>2</sub>/N<sub>2</sub> (N2 flow on the cathode was stopped during measurement). It should be noted that the previous work reported a strong correlation between  $H_2/N_2$  potential cycling stress and real-drive cycle conditions.<sup>[16a]</sup> Moreover, this work revealed that oxygen partial pressure does not have a significant impact on the stress test, which indicates that our  $H_2/N_2$ stress test is a suitable proxy for practical operating conditions. [16] The ECSA was estimated from the desorption peak of the CVs using a constant charge of 210  $\mu\text{C/cm}^2\text{Pt}$ . The plotted CV data were corrected for the hydrogen gas crossover. The ohmic resistance was estimated from the x-axis intercept in the electrochemical impedance Nyquist plot measured in the range of 100 kHz to 100 Hz at each current density. The voltage cycling tests were carried out under  $H_2/N_2$  (anode/cathode) at atmospheric conditions, 80 °C, 100% RH. The potential was cycled between 0.6 and 1.0 V in a square wave with holding times of 2 s at each potential. For all MEA experiments, a cycle count of 6000 cycles was chosen. CVs were measured every 1500 cycles.

Density Functional Theory Calculations: DFT calculations were carried out using the opt-type Perdew—Burke–Ernzerhof (optPBE) formulation of the generalized gradient approximation (GGA) with the projected augmented wave (PAW) method, as implemented in the Vienna ab initio Simulation Package (VASP).<sup>[27]</sup> A plane-wave basis set cutoff energy of 520 eV was used in all calculations. More details on the atomistic DFT calculations are provided in the Supporting Information.

# **Supporting Information**

Supporting Information is available from the Wiley Online Library or from the author.

**ADVANCED** SCIENCE NEWS

www.advancedsciencenews.com



www.afm-journal.de

# Acknowledgements

This work was primarily supported by Robert Bosch LLC. Additional support was provided by the Basic Science Research Program through the National Research Foundation of Korea (NRF) funded by the Ministry of Education (2020R1A6A3A03038630). Graphene powder production was supported by the National Science Foundation Scalable Nanomanufacturing Program (NSF CMMI-1727846 and NSF CMMI-2039268) and the National Science Foundation Future Manufacturing Research Grant Program (NSF CMMI-2037026). This work made use of the EPIC facility of the Northwestern University NUANCE Center, which is supported by the Soft and Hybrid Nanotechnology Experimental (SHyNE) Resource (NSF ECCS-1542205), the Materials Research Science and Engineering Center (NSF DMR-1720139), the State of Illinois, and Northwestern University. M.S. was supported by the Department of Defense (DoD) through the National Defense Science and Engineering Graduate (NDSEG) Fellowship Program. J.M., C.J., and S.K. were supported by Robert Bosch LLC.

# **Conflict of Interest**

S.K. and J.M. are inventors on a U.S. patent issued by Robert Bosch GmbH related to this work (US 11,145,875 B2, 12 October 2021). The other authors declare that they have no competing interests.

### **Author Contributions**

K.-Y.P. and M.E.S contributed equally. K.-Y.P. and M.E.S. primarily implemented this study. U.B. conducted electrochemical MEA characterization and data evaluation. E.H. performed the MEA sample preparation. J.M. and S.K. carried out the DFT calculations. J.R.D. synthesized the graphene/EC powder. S.K. and M.C.H. conceived the overall project. C.J. and L.C.S. were responsible for providing direction and advice for electrochemical analysis. All the authors contributed to writing the manuscript.

## **Data Availability Statement**

The data that support the findings of this study are available from the corresponding author upon reasonable request.

### **Keywords**

accelerated stability tests, electrochemical surface area, membrane electrode assemblies, proton exchange membrane fuel cells, rotating disc electrodes

Received: May 7, 2022 Revised: July 11, 2022 Published online: August 18, 2022

- A. Kirubakaran, S. Jain, R. K. Nema, Renewable Sustainable Energy Rev. 2009, 13, 2430.
- [2] Y. Wang, K. S. Chen, J. Mishler, S. C. Cho, X. C. Adroher, Appl. Energy 2011, 88, 981.
- [3] Y. Jiao, Y. Zheng, M. Jaroniec, S. Z. Qiao, Chem. Soc. Rev. 2015, 44, 2060
- [4] S. Sui, X. Wang, X. Zhou, Y. Su, S. Riffat, C.-j. Liu, J. Mater. Chem. A 2017, 5, 1808.

- [5] R. Borup, J. Meyers, B. Pivovar, Y. S. Kim, R. Mukundan, N. Garland, D. Myers, M. Wilson, F. Garzon, D. Wood, P. Zelenay, K. More, K. Stroh, T. Zawodzinski, J. Boncella, J. E. McGrath, M. Inaba, K. Miyatake, M. Hori, K. Ota, Z. Ogumi, S. Miyata, A. Nishikata, Z. Siroma, Y. Uchimoto, K. Yasuda, K.-i. Kimijima, N. Iwashita, Chem. Rev. 2007, 107, 3904.
- [6] P. Ferreira, Y. Shao-Horn, D. Morgan, R. Makharia, S. Kocha, H. Gasteiger, J. Electrochem. Soc. 2005, 152, A2256.
- [7] E. Guilminot, A. Corcella, F. Charlot, F. Maillard, M. Chatenet, J. Electrochem. Soc. 2007, 154, B96.
- [8] N. Tian, Z.-Y. Zhou, S.-G. Sun, Y. Ding, Z. L. Wang, Science 2007, 316, 732.
- [9] D. Fofana, S. K. Natarajan, J. Hamelin, P. Benard, Energy 2014, 64, 398.
- [10] S. T. Thompson, B. D. James, J. M. Huya-Kouadio, C. Houchins, D. A. DeSantis, R. Ahluwalia, A. R. Wilson, G. Kleen, D. Papageorgopoulos, *J. Power Sources* 2018, 399, 304.
- [11] a) E. Padgett, V. Yarlagadda, M. E. Holtz, M. Ko, B. D. A. Levin, R. S. Kukreja, J. M. Ziegelbauer, R. N. Andrews, J. Ilavsky, A. Kongkanand, D. A. Muller, J. Electrochem. Soc. 2019, 166, F198; b) X. Tuaev, S. Rudi, P. Strasser, Catal. Sci. Technol. 2016, 6, 8276.
- [12] a) N. Cheng, M. N. Banis, J. Liu, A. Riese, X. Li, R. Li, S. Ye, S. Knights, X. Sun, Adv. Mater. 2015, 27, 277; b) M. Karuppannan, Y. Kim, S. Gok, E. Lee, J. Y. Hwang, J.-H. Jang, Y.-H. Cho, T. Lim, Y.-E. Sung, O. J. Kwon, Energy Environ. Sci. 2019, 12, 2820; c) Z.-Z. Jiang, Z.-B. Wang, Y.-Y. Chu, D.-M. Gu, G.-P. Yin, Energy Environ. Sci. 2011, 4, 728; d) Y. Shao, S. Zhang, C. Wang, Z. Nie, J. Liu, Y. Wang, Y. Lin, J. Power Sources 2010, 195, 4600; e) Y. Zhou, K. Neyerlin, T. S. Olson, S. Pylypenko, J. Bult, H. N. Dinh, T. Gennett, Z. Shao, R. O'Hayre, Energy Environ. Sci. 2010, 3, 1437; f) D. Deng, L. Yu, X. Chen, G. Wang, L. Jin, X. Pan, J. Deng, G. Sun, X. Bao, Angew. Chem., Int. Ed. 2013, 52, 371.
- [13] C.-Y. Ahn, W. Hwang, H. Lee, S. Kim, J. E. Park, O.-H. Kim, M. Her, Y.-H. Cho, Y.-E. Sung, Int. J. Hydrogen Energy 2018, 43, 10070.
- [14] A. Korovina, Y. Garsany, A. Epshteyn, A. P. Purdy, K. More, K. E. Swider-Lyons, D. E. Ramaker, J. Phys. Chem. C 2012, 116, 18175.
- [15] a) D. Higgins, P. Zamani, A. Yu, Z. Chen, Energy Environ. Sci. 2016, 9, 357; b) S. Shahgaldi, J. Hamelin, Carbon 2015, 94, 705.
- [16] a) S. Stariha, N. Macauley, B. T. Sneed, D. Langlois, K. L. More,
  R. Mukundan, R. L. Borup, J. Electrochem. Soc. 2018, 165, F492;
  b) W. Bi, Q. Sun, Y. Deng, T. F. Fuller, Electrochim. Acta 2009, 54, 1826.
- [17] K.-Y. Park, J.-M. Lim, N. S. Luu, J. R. Downing, S. G. Wallace, L. E. Chaney, H. Yoo, W. J. Hyun, H.-U. Kim, M. C. Hersam, Adv. Energy Mater. 2020, 10, 2001216.
- [18] Y. T. Liang, M. C. Hersam, J. Am. Chem. Soc. 2010, 132, 17661.
- [19] M. S. Dresselhaus, A. Jorio, R. Saito, Annu. Rev. Condens. Matter Phys. 2010, 1, 89.
- [20] a) L. Vicarelli, S. J. Heerema, C. Dekker, H. W. Zandbergen, ACS Nano 2015, 9, 3428; b) Ç. O. Girit, J. C. Meyer, R. Erni, M. D. Rossell, C. Kisielowski, L. Yang, C.-H. Park, M. Crommie, M. L. Cohen, S. G. Louie, Science 2009, 323, 1705; c) J. L. Achtyl, R. R. Unocic, L. Xu, Y. Cai, M. Raju, W. Zhang, R. L. Sacci, I. V. Vlassiouk, P. F. Fulvio, P. Ganesh, Nat. Commun. 2015, 6, 6539.
- [21] J. Zhao, Z. Tu, S. H. Chan, J. Power Sources 2021, 488, 229434.
- [22] E. B. Secor, T. Z. Gao, A. E. Islam, R. Rao, S. G. Wallace, J. Zhu, K. W. Putz, B. Maruyama, M. C. Hersam, Chem. Mater. 2017, 29, 2332.
- [23] S. Sharma, B. G. Pollet, J. Power Sources 2012, 208, 96.
- [24] G. S. Harzer, J. N. Schwämmlein, A. M. Damjanović, S. Ghosh, H. A. Gasteiger, J. Electrochem. Soc. 2018, 165, F3118.
- [25] V. Komanicky, K.-C. Chang, A. Menzel, H. You, X. Wang, D. Myers, N. Markovic, ECS Trans. 2019, 1, 167.
- [26] J. I. Choi, A. Abdelhafiz, P. Buntin, A. Vitale, A. W. Robertson, J. Warner, S. S. Jang, F. M. Alamgir, Adv. Funct. Mater. 2019, 29, 1902274.
- [27] a) G. Kresse, J. Furthmüller, Comput. Mater. Sci. 1996, 6, 15;
   b) G. Kresse, J. Hafner, Phys. Rev. B 1993, 47, 558;
   c) G. Kresse,
   D. Joubert, Phys. Rev. B 1999, 59, 1758.